# True Two-Dimensional Molecular Studies of Electrospray Plumes

## IEPC-2025-423

*For the 39th International Electric Propulsion Conference*
*Imperial College London, London, United Kingdom*
*14–19 September 2025*

Zach Ulibarri[1], Giuliana Hofheins[2], Savera Sahai[3], and Elaine Petro[4]
*ASTRA Lab, Sibley School of Mechanical & Aerospace Engineering, Cornell University, Ithaca NY 14850, USA*

## I. Introduction

Electrospray thrusters are an emerging electric propulsion (EP) technology that operate by electrostatically firing ions from vacuum stable ionic liquids at exceptionally high velocity. These electrospray systems have the potential to be among the most efficient propulsion sources available while also providing a level of precise thrust control that is difficult or impossible to achieve with other EP sources [1]. Despite this potential, actual electrospray propulsion sources are observed to be lifetime-limited due to electrical shorting, often thought to be the result of propellant accumulation from off-axis, angular emission onto source geometries and surfaces [2–4]. Further, actual thruster designs are observed not to reach their full mass efficiency, with significant portions of the propellant not producing thrust or producing it at significantly lower amplitude than predicted [5–8]. This missing mass may largely be the result of trimers or typically undesirable heavy mass clusters within the emitted plume itself undergoing fragmentation, and angle-dependent molecular composition differences may help shed light on this phenomenon, especially with an eye towards any ability to characterize the presence of neutrals moving in the plume [9–13]. Thus, a better understanding of the angular firing properties of the ejecta plumes, especially with respect to molecular composition, is important to the long-term realization of the full potential of these EP sources.

While some limited two-dimensional studies exist (e.g., [14–16]), experimental measurements of electrospray systems are typically taken uncritically along the axis of the emitter tip. Some important works studying angular phenomena of the electrospray plumes are given in Refs. [14–18]. However, even these angular studies are typically limited to only one degree of freedom in rotation or lack the ability to study the molecular feature of the plumes directly. Schroeder et al. 2023 [17] and Jia-Richards [18] are of particular note for providing angular molecular quantification in one dimension. However, emitters are known to often fire off-axis and exhibit two-dimensional phenomena, sometimes as a function of extraction potential [15, 17, 18]. Many of the angular features, most notably emitted ion molecular variation, of the electrospray plume are critical to constraining theoretical models of the plume, especially as regards missing mass and propellant buildup and shorting [9]. Thus, carefully-controlled high resolution datasets from well-characterized emitter geometries delineating the angular features of vacuum electrospray plumes are of high value to modeling efforts [5] and to providing better understanding of the problems facing modern electrospray thrusters.

We have recently demonstrated [19] a novel and simple method for the direct, two-dimensional study of electrospray plumes utilizing an externally wetted tungsten needle with the ionic liquid 1-Ethyl-3-methylimidazolium tetrafluoroborate (EMI-BF4). Using a commercial off-the-shelf goniometer, angular time-of-flight (TOF) compositional measurements were performed across the beam's peak-amplitude center line, finding significant variation in the relative abundance of propellant molecular composition across the plume structure. Nonetheless, while this study leveraged the two-dimensional capabilities of the gonimetric system to ensure that the compositional profile scanned across the true peak-amplitude beam center line, it was in essence still a one-dimensional study; it only considered composition across a single beam slice.

Here we present a systematic study of a vacuum electrospray plume in two angular dimensions with a carefully-characterized emitter geometry. Using computer-controlled motors to manipulate a goniometer in-vacuo, TOF data was

---

[1]Postdoctoral Associate, ASTRA Lab, Sibley School of Mechanical & Aerospace Engineering, zulibarri@cornell.edu
[2]PhD Student, ASTRA Lab, Sibley School of Mechanical & Aerospace Engineering, gch72@cornell.edu
[3]Master's of Science Graduate, ASTRA Lab, Sibley School of Mechanical & Aerospace Engineering, ss4328@cornell.edu
[4]Assistant Professor, ASTRA Lab, Sibley School of Mechanical & Aerospace Engineering, epetro@cornell.edu

taken in two-degree resolution in two dimensions across an externally-wetted tungsten needle vacuum electrospray source loaded with EMI-BF4 over a one-hour experiment. Importantly, immediately after firing, the source was imaged with a laser profilometer to recover an accurate three-dimensional model of the precise location of the needle emitter in the extractor circle to further aid in the direct comparison of this data to modeling efforts. The particular assembly studied had significant offset between the extractor circle's center and the needle's tip.

As with our previous work, we find significant molecular variation across the plume as a function of angle, but with the new two-dimensional capabilities, clear asymmetries are observed in the plume's molecular composition. As expected, the resultant propellant beam fires off-axis in the direction of the needle's offset towards the nearest extractor edge. The lighter monomers are also preferentially skewed in that direction as well, resulting in a shifted monomer:dimer ratio that is stronger in the direction of the closest extractor edge. Trimers and heavier mass species are deflected less, and tend towards an axis closer to that of the emitter geometry.

Further, an unexpected current signal that is evidently the result of neutrals, secondary species, and/or other particles that are unaffected by the time-of-flight (TOF) high voltage gate pulse is observed in a narrowly-defined beam. Naemura and Takao [10] have recently reported direct measurement of neutral species in a somewhat similar manner, and thus it is thought that this signal represents a significant amount of neutral species with kinetic energy sufficient to trigger an MCP response [9]. The feature is well-defined in the two-dimensional parameter space, decreasing the likelihood that it is composed of secondaries or other exotic species. We find that this feature is slightly off-axis from, but overlapping with, the larger ion plume. In this particular study, it accounts for up to $\frac{1}{3}$ of the detector signal at its peak location. These results may have important implications for the missing mass inefficiencies observed for thruster designs and the lifetime-limiting buildups observed with long duration firing of electrospray thrusters.

## II. Experimental Setup

The goniometer system used in the present study is detailed in Ref. [19], and further details of the TOF setup are given in Ref. [20]. The in-vacuo hardware used in the present study is not meaningfully different from Ref. [19], but outside of the chamber, computer-controlled motors have been employed to automate movement of the goniometer in both directions. Software-defined serpentine scans were taken starting in the negative X and Y angles (that is, the bottom-left of the plots presented here). The serpentine scan holds the Y constant while sweeping across in X before increasing Y by one cell step and then scanning backwards across X. The software can be programmed to run custom software at each position, and for simple current measuring, such as presented in IEPC-2025-46 [21] and IEPC-2025-426 [22], the process is fully automated. However, for TOF measurements, the signal intensity varies so greatly over the 2D parameter space that a human is required to manually adjust the oscilloscope window sensitivity at each stop. To accomplish this, the software moves to the specified location and throws a pop-up window for the user. The user may manually enter data such as source meter unit (SMU) voltage or current or general notes and reminders, but this is strictly optional. When the user has adjusted the scope to a proper resolution, they close the pop-up window and the software automatically takes a number of TOF curves. For the data presented here, each TOF curve contains 1000 averaged spectra triggered off the high voltage gate pulses to improve SNR, and two averaged recordings were taken at each angle. Once completed, the software moves the motors to the next angle and the process is repeated.

Whereas in Ref. [19] the microchannel plate (MCP) voltage baseline was treated as a confounding factor and eliminated through subtraction, here we recognize it as an important fundamental feature of the emission. It suggests that significant populations of high-velocity neutral particles are present within a narrowly-defined region of the plume, although the feature could also be the result of secondaries or any other particles that are not deflected by the high voltage TOF gate.

Because this slight difference in analysis is critical to understanding the results presented here, it is worth reiterating and updating the methods used to quantify the various molecular contributions to the plume. Fig. 1, based on Fig. 2 of Ref. [19], details this method. As before, current for monomers, dimers, and trimers are measured as the voltage rise between bounds identified by exponentially modified Gaussians (EMGs) fitted to the derivative of the data smoothed by a Gaussian blur (in this case of width 30 in the index domain). Whereas before the found indices were averaged across the entire dataset to find a single set to use, here they were chosen from a single exemplar spectrum for expediency, as the slight changes between individual spectra do not have a meaningful impact on the results presented here. As before, the voltage rise in between each species is taken to be fragmenting species. For example, between the upper monomer bound and the lower dimer bound, the voltage rise is taken as the fragmenting dimer population. However, it should be noted that this is very much a simplification, as much higher mass cluster groups and even droplets may contribute ions in these regions as a result of collisions [9]. As before, the voltage rise from the upper trimer bound to an arbitrary point
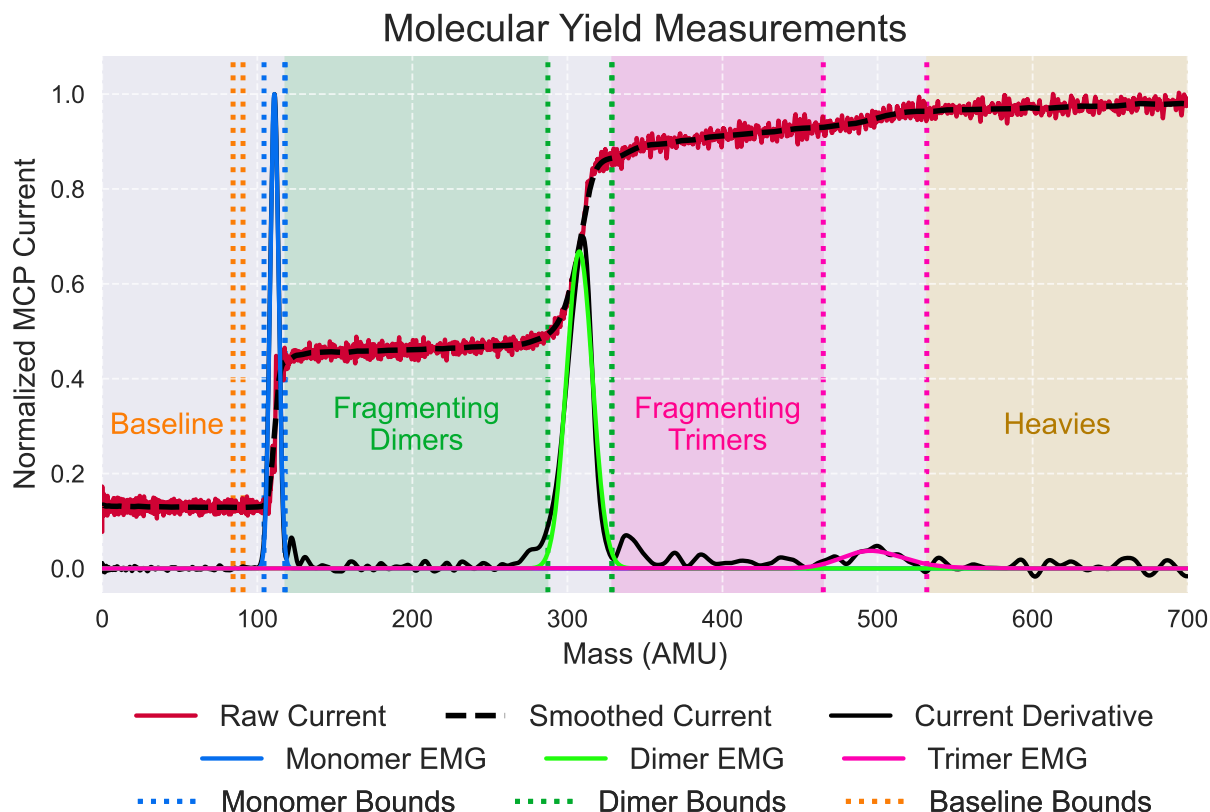
**Fig. 1** **A description of how the molecular yields for each species are determined. While mostly the same as Fig. 2 of Ref. [19], the key difference is that there is now an additional pair of baseline bounds to determine the baseline MCP voltage bias by averaging the MCP signal between them. This results in a measure of the voltage offset for each spectrum, which here is about 13% of the normalized signal. While Ref. [19] treated this as a confounding factor and simply subtracted it out, here we recognize this as an important feature that gives vital information about neutrals, secondaries, or other species that are not deflected by the high voltage TOF gate.**

near mass 2800 AMU at the end of the recorded data is taken as the heavy particle or droplet yield. Lastly, a new set of bounds called the baseline bounds were arbitrarily placed before the monomer lower bound to determine the baseline MCP bias for each spectrum, where the MCP signal between the baseline bounds was averaged to find the MCP bias. The bounds are chosen very near each other close to the monomer signal because in the high-off-axis spectra, a small voltage drop is observed near the gate pulse at the beginning of the data. The placement of these bounds was visually selected to ignore this confounding factor and produce a uniform baseline for all of the data.

It should also be noted that a "true" MCP bias of 12.4 mV was observed at high-off-axis angles, which is thought to be the result of secondary species impacting chamber walls[23–25], or perhaps an electronics artifact. This value was subtracted from all signals before any other processing was done to produce data centered at the "true" zero voltage. The subtraction does not meaningfully alter any of the results presented here.

Before the data presented here was taken, the needle was conditioned by firing for approximately half an hour on an unrelated experiment. An initial scan was then performed in 5° resolution over the entire GOH-40B35 goniometer parameter space of ±20° in X and ±15° in Y to deduce an approximate plume center angle. This initial scan took approximately 15 minutes. Stable output current was observed, so a high resolution scan to take the data presented here was taken in 2° resolution across X from -15 to +19 and Y from -15 to +13 over almost exactly one hour. Further data was taken out to Y = +11 over an additional 20 minutes. While visible TOF data was observed on the scope out to approximately Y = +11, the data is sparsely above the noise floor and so has not been analyzed. We thus only present

data over the ranges of -11 to +19 in X and -15 to +5 in Y, as even here the corners of the data have low SNR data that is difficult to draw meaningful conclusions from.

### A. Laser profilometry

A Keyence VK-X260 laser profilometer with a 10x objective at the Cornell Center for Materials Research was used to image the source immediately after the experiment was performed. This instrument, which has a resolution of 659 nm per pixel, was used to image the emitter down the needle axis immediately after data was taken. This provides highly resolved three-dimensional structure of the precise emitter configuration, most notably the position of the emitter within the circular extractor cutout. Fig. 2 shows results from the laser profilometer, including the X and Y profile scans across the needle's center. The needle used here has a radius of curvature of ~8.5$\mu m$.
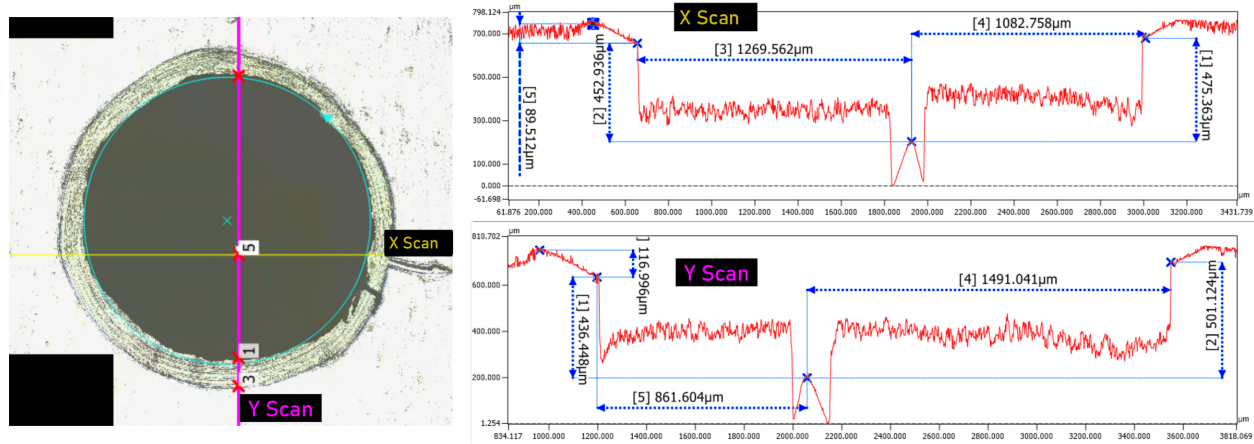


**Fig. 2    Results from the laser profilometer of the emitter assembly used in this study. The needle tip is significantly off-center from the extractor circle in both X and Y, but the error is greater in Y. From the laser profile, a full 3D reconstruction was created. An STL file will be available for the final journal publication of this data.**

## III. Results

Fig. 3 (A) shows the output voltage of the MCP and TDC-30 transimpedance amplifier at each goniometer angle, less the true MCP bias as described in Sec. II. As described in Ref. [19], because of the dual-axis goniometer system's ability to dramatically increase SNR, we were forced to turn down our MCP amplification voltage to 900 volts (from the nominal value of 1 kV) to fully recover the signal. Unfortunately Hamamatsu was unable to provide estimates for MCP gain at this potential, and thus we cannot provide absolute current measurements. A black dot is placed at X = 0 and Y = 0. Fig. 3 (C) shows the output current from the Keithley 2675A source meter unit (SMU), from which it can be seen that while some fluctuation in output current is present, it is largely stable during the ~60 minutes of firing time that the data was taken over. Fig. 3 (B) shows the MCP current normalized to the SMU output. That is, (B) is the signal from (A) divided by the signal in (C) to account for variation in the emitted current over time. Data from (C) was taken as the average output current over a 10 second period after the goniometer arrived at the specified angle, which roughly corresponds to the period over which TOF data was taken at each location. It is surprising that Fig. 3 (B) shows more varied structure than (A), so we present both for readers to draw their own conclusions. Both the normalized and raw MCP currents have a maximum signal at about X = 5° and Y = -7 or -9°. Fig. 3 (D) shows the MCP baseline bias in volts as a function of goniometer angle, which again is the average voltage between the baseline indices as shown in Fig. 1. This signal is a baseline or background bias voltage that affects the entirety of each spectra at the specified angle. Whereas (A) and (B) have apparent maxima around X = 5° and Y = -7 or -9°, (D) displays a center that is shifted slightly downward at approximately X = 5° and Y = -11°, where it has a maximum of 200 mV, approximately $\frac{1}{3}$ of the MCP voltage (A) at that point.

Figs. 4 (A) through (E) display the fractional contributions of each quantified species in the TOF spectra. These are defined as the voltage rise between the relevant bounds in Fig. 1 divided by the total voltage rise across the entire spectrum, less the true MCP bias of 12.4 mV as described in Sec. II. This normalization is functionally equivalent to
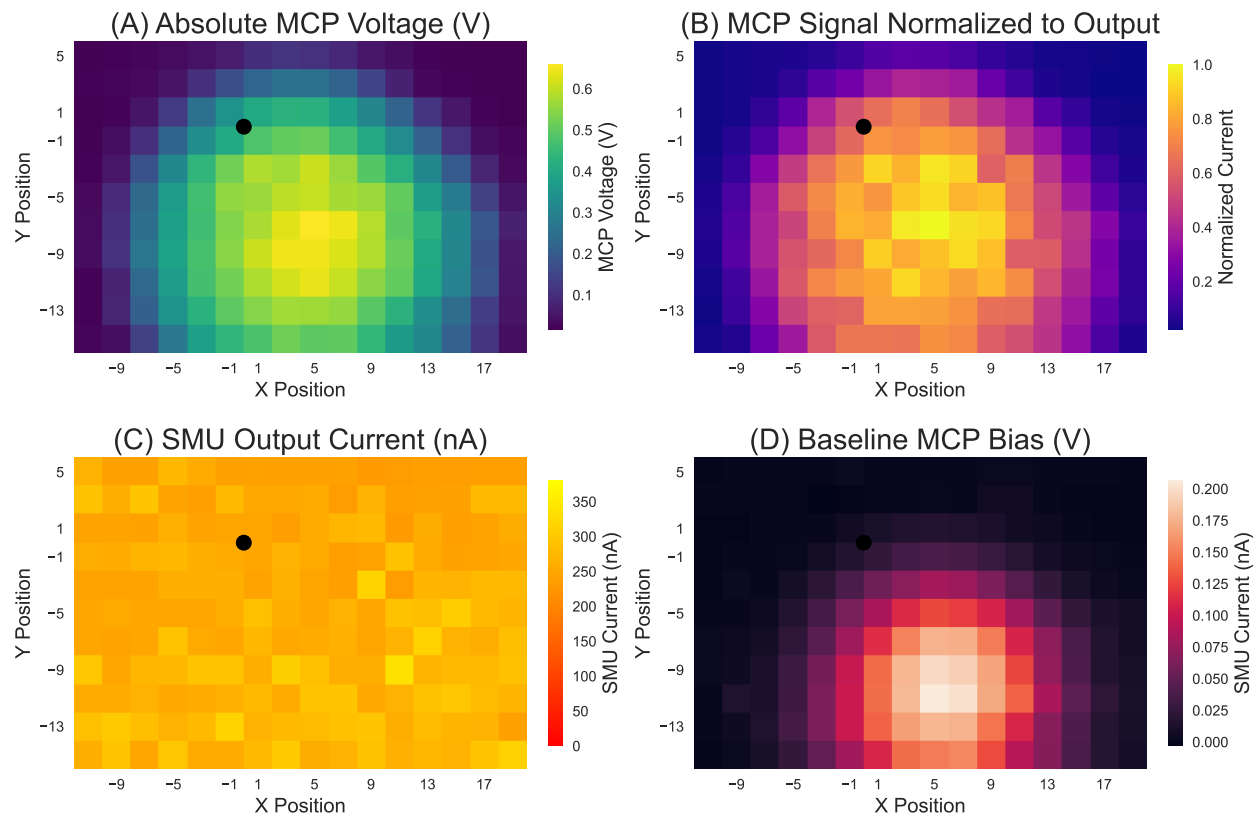
**Fig. 3 (A) Microchannel plate (MCP) voltage measured as a function of goniometer angle. An evident center is present around X = 4 or 5 and Y = -7. A black dot is centered at X = 0 and Y = 0. As with the needle displacement the center is further offset down in Y than it is to the right in X. (B) MCP current normalized to source-meter unit (SMU) output current, which also has a center roughly at X = 4 or 5 and Y = -7. (C) Output current (average of ~10 seconds of data) of the SMU at each angle. While some fluctuation is present, it is largely uniform. (D) The baseline MCP bias in volts at each angle. This signal is significantly more narrowly-defined than the rest of the plume and appears to be shifted downward to Y = -11°. It suggests the presence of high-velocity neutrals that could trigger an MCP response, or other species such as secondaries that are not deflected by the high-voltage TOF gate.**

dividing each species's voltage rise by Fig. 3 (A) to provide a fractional abundance of each species at the specified angle.

Fig. 4 (A) shows the monomer fractional yield, with a clear ring structure evidently centered at X = 5 and Y around -7, which corresponds to the center of the total current yield given by Fig. 3 (A). The ring shows a decreased intensity above Y =0, but it is slightly canted; the decrease is asymmetric in X, with higher intensities continuing on the right side slightly higher than the left. There is a clear depletion of monomers in the center of the plume, a feature that was also observed in the one-dimensional results of Ref. [19].

Fig. 4 (B) shows the dimer fractional yield. While it displays a ring structure similar to that of the monomers, it is more muddled, with a higher abundance in the center despite brighter intensity in the ring structure. This is also similar to the one-dimensional results in Ref. [19]. It is of particular note that the dimer fraction shows a clearly increased intensity on the left side of the plot between X = -5 and X = -9 that is not reciprocated on the right side. It is difficult to pinpoint a dimer feature center by eye, but it appears to be shifted slightly further up than the monomer feature.

Figs. 4 (C) and (D) show the trimer and heavy molecule fractional yields respectively. Both show a markedly different center location than the monomer and dimer populations, with centers roughly around X = 3 and Y = -3. Both also exhibit increased intensity along the top part of the ring structure.

Fig. 4 (E) shows the putative neutral fractional yield. The feature appears to have a center at approximately X = 7 and Y = -11, which is one cell to the right and two cells down from the max signal intensity of the baseline MCP bias
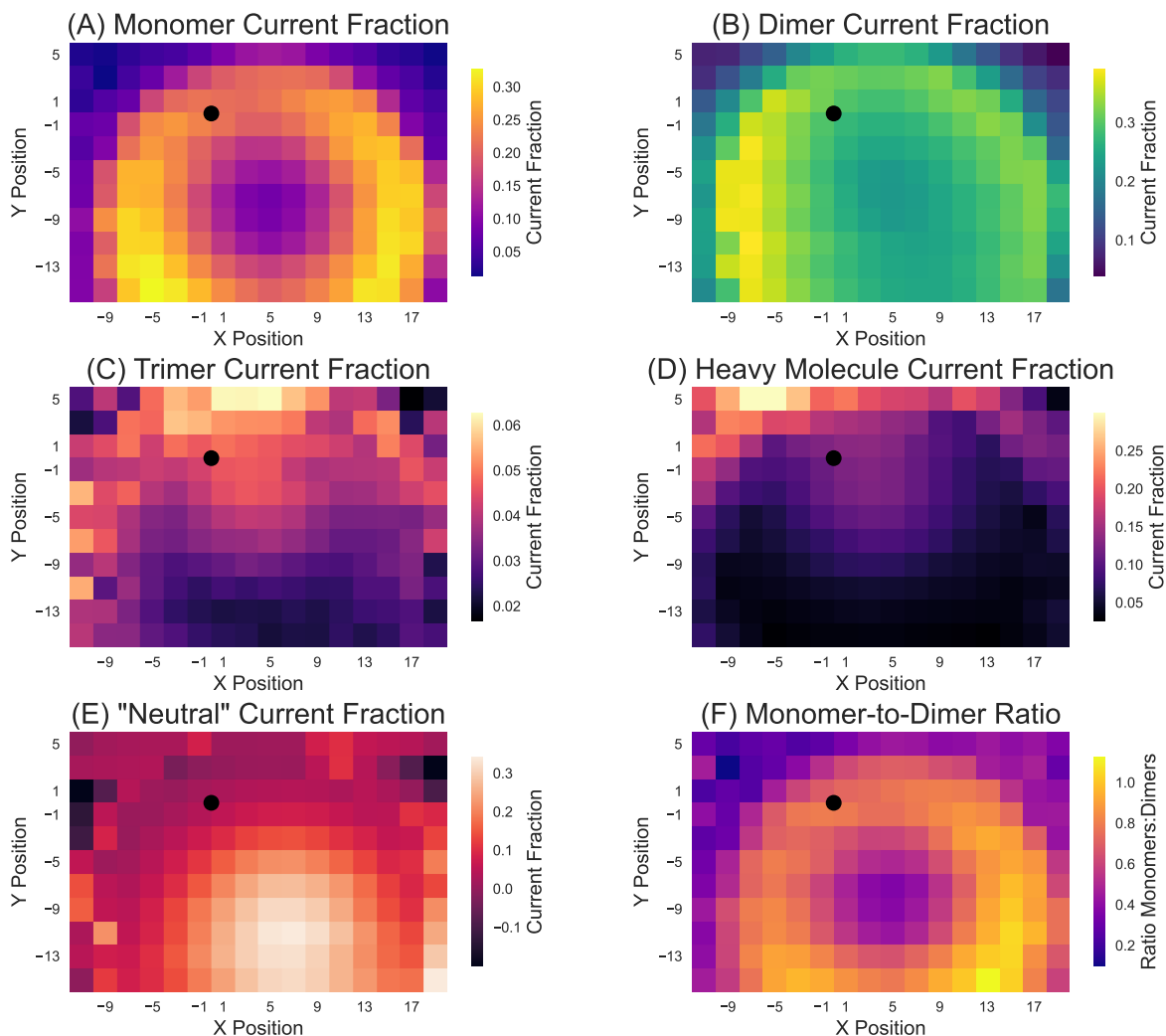
**Fig. 4** **(A) through (E) display the fractional contributions of each quantified species in the TOF spectra. These are defined as the voltage rise between the relevant bounds in Fig. 1 divided by the total voltage rise across the entire spectrum, less the true MCP bias of 12.4 mV as described in Sec. II. This normalization is functionally equivalent to dividing each species's voltage rise by Fig. 3 (A) to provide a fractional abundance of each species at the specified angle.**

feature in Fig. 3 (D).

Fig. 4 (F) shows the monomer-to-dimer ratio of the data, with a clear asymmetry present. The bottom right side of the ring structure shows a markedly brighter intensity than the rest of the ring. This could be interpreted as the lighter monomers being more easily deflected towards the nearest extractor edge.

It is important to note that the heatmap color legend scales vary dramatically between each plot in Fig. 4, with the monomers and dimers covering ranges up to approximately $\frac{1}{3}$ of the plume, while the trimer feature is significantly weaker, ranging only up to about 6 % of the plume's contents.

Fig. 5 shows the two fractional yields of the fragmenting species, with fragmenting dimers in (A) and fragmenting trimers in (B). It should again be stressed that this is a gross oversimplification in terminology, as higher-order species may fragment and contribute to these regions as well. The fragmenting dimer population in Fig. 5 (A) shows a mostly featureless center area with around 10% of the total yield. A slight decrease in abundance is present around X = 5 and Y = -5, dropping to around 8% of the yield. In contrast, the fragmenting trimer population shows a clearly defined center spot at X = 3 and Y = -5, where it rises to approximately 20% of the total current yield.
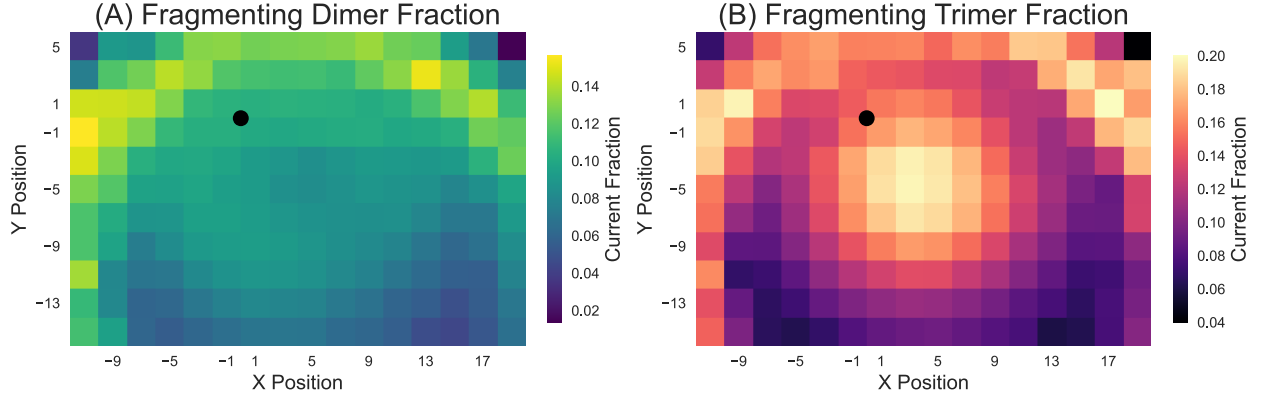
6

**Fig. 5  Fractional current contributions of the fragmenting species as defined in Fig. 1. (A) shows the fragmenting dimer current, with a largely featureless center field. (B) shows a clear center structure present in the fragmenting trimer population.**

## IV. Discussion

A simple and intuitive means of explaining the results of Fig. 4 is that, owing to their comparatively low mass, the monomers are pulled more strongly in the positive X and negative Y direction than the other charged species since that is the direction towards the closest extractor edge. It is interesting, however, that the neutrals appear to be yet further away from the centers of any other feature. Whereas the monomers are centered at approximately X - 5 and Y = -7, the neutrals are centered much lower, at Y = -11 and slightly further to the right. While it could be expected that the monomers would be deflected further to the bottom right (towards the nearest extractor edge) than the dimers and trimers due to their lower mass, one would not naively expect the neutrals to be the population that is most deflected away from the emitter center axis. This observation may be ripe for modeling efforts to better explain.

The neutrals presented here are not well-understood, and they could be the result of secondary ions created from the impact of primary plume constituents with downstream experimental geometries. Indeed, such secondary ions are very likely the source of the "true" MCP bias observed in far-off-axis TOF data. However, it is difficult to explain why such secondaries would be so strongly present under such a narrowly defined region of the plume, and one that is only slightly off-axis from the bulk ionized content. Naemura and Takao [10] have recently reported direct observation of neutrals in a similar method, so it is believed that this baseline MCP signal represents a significant portion of the plume mass is being carried away by neutral species. Such species could be the result of fragmentation that produces ions detected in the fragmenting dimer or fragmenting trimer regions.

In this dataset, the neutrals account for as much as $\frac{1}{3}$ of the MCP signal at the neutral beam max intensity angle. Because it is difficult to quantify the current output of the MCP for such species owing to their unknown velocity and unspecified potential cluster masses, to say nothing of the MCP response at the decreased amplification of 900 V, quantification of the total contribution to the mass flow for these species will take further work.

It is important to remember that these results represent a single experiment with a single emitter, and they should not be taken to be perfectly emblematic of the entire field of electrospray technology. Further, it is also important to remember that the emitter geometry studied here featured a needle that was significantly offset from the extractor axis. The rudimentary source utilized in this experiment is far from the precision emitters employed by actual electrospray propulsion sources, and future studies will take greater care to properly center the needle.

It might be of particular interest to use the system presented here to perform direct comparisons between externally wetted emitters [26], precision micromachined emitters [4], and additively manufactured emitters [22, 27] of similar geometry.

It is also important to remember that the data presented here was taken over an hour of operation, meaning that the plume may have undergone some level of change during the experiment. Because the data was taken starting in the negative X and Y (that is, the bottom left of each plot) and then took a serpentine pattern scanning across the full range of X angles for each Y angle, it is expected that any variation in data as a result of emission characteristics changing over time should manifest as shifts in the data in the Y-direction.

The monomer fraction shown in Fig. 4 (A) shows a clear ring structure with higher abundance in the lower Y values.

However, it also displays asymmetry in X, with the right side (higher positive X values) showing a higher abundance for higher values of Y than the left side. This would seem to suggest that the increased monomer intensity in the lower part of the plot is not a result of time-dependent emitter characteristics, but is rather a result of true asymmetries in the steady-state plume. Giving credence to this claim is the structure of the dimer fraction shown in Fig. 4 (B), which exhibits a markedly increased intensity in the left side of the ring structure compared to the right side. As this intensity feature is only observed in the negative X across most values of Y, it strongly suggests that the plume was indeed quite stable over the firing time. This is further suggested by the relative stability in output current as shown in Fig. 3 (C).

It may be of interest that the monomer-to-dimer ratio shown in Fig. 4 (F) has one particularly bright spot of the two-degree resolution data where the ratio rises above unity. In the one-dimensional data of Ref. [19], a small patch of this ratio on one side of the data was observed to rise above unity over approximately 3 degrees of parameter space. This is very likely a coincidence, but we note the oddly similar result.

The results presented here are the result of a preliminary analysis, and we will soon have more carefully detailed plume characteristics, including mass flow as a function of angle and mathematically defined center axes for the structures of each species fraction.

Aside from the scientific value of this data, as we note in Ref. [19], the goniometer system is incredibly useful as a laboratory utility. It can be used to dramatically increase the SNR of emitter firing off-axis, and the new control software developed for the motorized system allows for rapid and accurate two-dimensional data collection. In particular, it was critical to the observation and recording of a transient second emission site in IEPC-2025-426 [22] and in particular to record the incredibly thin LNIS [13] emission line in IEPC-2025-46 [21].

We also have created a preliminary graphical user interface (GUI) for the motorized control system which allows for rapid and intuitive movement of the goniometers in-vacuo. It also can be operated with a wireless controller so that a user can remotely manipulate both axes of the goniometer. This remote control was of particular value to IEPC-2025-46 [21], where the fast-moving thin emission would have been extremely difficult to keep track of by hand. We intend to make the GUI software available to the community when it is ready in a near-future publication.

## V. Acknowledgements

## References

[1] Krejci, D., and Lozano, P., "Space propulsion technology for small spacecraft," *Proceedings of the IEEE*, Vol. 106, No. 3, 2018, pp. 362–378.

[2] Thuppul, A., Collins, A., Wright, P., Uchizono, N., and Wirz, R., "Mass flux and current density distributions of electrospray plumes," *Journal of Applied Physics*, Vol. 130, No. 10, 2021.

[3] Krejci, D., Mier-Hicks, F., Thomas, R., Haag, T., and Lozano, P., "Emission characteristics of passively fed electrospray microthrusters with propellant reservoirs," *Journal of Spacecraft and Rockets*, Vol. 54, No. 2, 2017, pp. 447–458.

[4] Krejci, D., and Lozano, P., "Micro-machined ionic liquid electrospray thrusters for Cubesat applications," *Proceedings of the 35th International Electric Propulsion Conference*, Electric Rocket Propulsion Soc., 2017, pp. 1–14.

[5] Smith, A. G., and Petro, E. M., "Propagating an electrospray emission model to array scales using particle-in-cell," *Journal of Propulsion and Power*, Vol. 40, No. 5, 2024, pp. 677–690.

[6] De Saavedra, B., Villegas-Prados, D., Wijnen, M., and Cruz, J., "Comparison between direct and indirect measurements for externally wetted electrospray thruster with adapted analytical balance," *Acta Astronautica*, Vol. 232, 2025, pp. 283–295.

[7] Natisin, M. R., Zamora, H. L., Holley, Z. A., Ivan Arnold, N., McGehee, W. A., Holmes, M. R., and Eckhardt, D., "Efficiency mechanisms in porous-media electrospray thrusters," *Journal of propulsion and power*, Vol. 37, No. 5, 2021, pp. 650–659.

[8] Lyne, C. T., Liu, M. F., and Rovey, J. L., "A simple retarding-potential time-of-flight mass spectrometer for electrospray propulsion diagnostics," *Journal of Electric Propulsion*, Vol. 2, No. 1, 2023, p. 13.

[9] Smith, A., Laws, N., Hofheins, G., and Petro, E., "Quantification of Missing Mass in Electrospray Ion Time-of-Flight Mass Spectrometry," *39th international electric propulsion conference*, Electric Rocket Propulsion Society, 2025.

[10] Naemura, M., and Takao, Y., "Direct detection of neutral species from ionic liquid electrospray thrusters in the purely ionic regime," *Review of Scientific Instruments*, Vol. 96, No. 7, 2025.

[11] Bendimerad, R., Tahsin, A. T. M., Yonas, A., Colucci, C., and Petro, E. M., "Investigating the chemical stability of electrospray plumes during particle collisions," *Journal of Propulsion and Power*, Vol. 40, No. 2, 2024, pp. 247–256.

[12] Tahsin, A. T. M., Bendimerad, R., Smith, A., Thill, S., Laws, N., and Petro, E. M., "Cross-sections for charge exchange and other collisional processes in electrospray plumes," *Journal of Propulsion and Power*, 2025, pp. 1–11.

[13] Bell, S., Tahsin, A. T. M., and Petro, E., "Experimental study of collision-induced dissociation for emi-im and emi-bf4," *International Electric Propulsion Conference. Toulouse, France: Electric Rocket Propulsion Society*, 2024.

[14] Ticknor, B., Miller, S., and Chiu, Y.-H., "Mass spectrometric analysis of the electrospray plume from an externally wetted tungsten ribbon emitter," *45th AIAA/ASME/SAE/ASEE Joint Propulsion Conference & Exhibit*, 2009, p. 5088.

[15] Wirz, R. E., "Electrospray thruster performance and lifetime investigation for the LISA mission," *AIAA Propulsion and Energy 2019 Forum*, 2019, p. 3816.

[16] Collins, A. L., Thuppul, A., Wright, P. L., Uchizono, N. M., Huh, H., Davis, M., Ziemer, J. K., Demmons, N. R., and Wirz, R. E., "Assessment of grid impingement for electrospray thruster lifetime," *Proceedings of the 36th International Electric Propulsion Conference, Vienna, Austria*, 2019, pp. 15–20.

[17] Schroeder, M., Gallud Cidoncha, X., Bruno, A., Jia-Richards, O., and Lozano, P., "Angular Properties of Ionic Liquid Electrospray Emitters," *AIAA SCITECH 2023 Forum*, 2023, p. 1408.

[18] Jia-Richards, O., "A Numerical Tool for Quantitative Analysis of Ionic-Liquid Ion Source Time-of-Flight Data," *International Electric Propulsion Conference. Toulouse, France: Electric Rocket Propulsion Society*, Electric Rocket Propulsion Society, 2024.

[19] Ulibarri, Z., and Petro, E., "Direct Two-Dimensional Goniometric Steering of Vacuum Electrospray Ion Beams for Angular Time-of-Flight Studies," *Accepted for Publication in Review of Scientific Instruments*, 2024. https://doi.org/10.48550/arXiv. 2409.13862.

[20] Cogan, S. P., Ulibarri, Z., Petro, E., and Hofmann, A. E., "Electrospray Mass Spectrometry for In-Orbit Biomolecule Analysis," *2023 IEEE Aerospace Conference*, IEEE, 2023, pp. 1–7.

[21] Bell, S., Chalmpes, N., Ulibarri, Z., Hofheins, G., Giannelis, E., and Petro, E., "Nanoparticle Ion Beam Interactions from a Liquid Nanoparticle Ion Source (LNIS)," *International Electric Propulsion Conference*, , No. 46, 2025.

[22] Kingsley, B., Chalmpes, N., Bell, S., Ulibarri, Z., Sobhani, S., and Petro, E., "Fabrication and Characterization of Two-Photon Printed Glass Electrospray Emitters with Architected Microporous Structure," *2025 39th International Electric Propulsion Conference*, 2025.

[23] Geiger, C. J., Hofheins, G., and Petro, E. M., "Secondary species investigation of low energy electrospray plume impacts," *Journal of Electric Propulsion*, Vol. 4, No. 1, 2025, p. 37.

[24] Hofheins, G. C., Ulibarri, Z., and Petro, E. M., "Electrospray propulsion time-of-flight secondary ion mass spectrometry diagnostic," *Review of Scientific Instruments*, Vol. 96, No. 6, 2025.

[25] Hofheins, G. C., Ulibarri, Z., and Petro, E. M., "Electrospray Secondary Ion Mass Spectrometry Diagnostic–Design and Preliminary Result," *International Electric Propulsion Conference. Toulouse, France: Electric Rocket Propulsion Society*, Vol. 1, 2024.

[26] Matsukawa, K., Nakashima, Y., Naemura, M., and Takao, Y., "Emission measurements and in-situ observation of ionic liquid electrospray thrusters with longitudinally grooved emitters," *Journal of Electric Propulsion*, Vol. 2, No. 1, 2023, p. 23.

[27] Chamieh, S., Geiger, C., D'Orazio, G., Sobhani, S., and Petro, E., "Additive Manufacturing and Characterization of Porous Glass Electrospray Emitters," *38th International Electric Propulsion Conference, Toulouse*, 2024.